Journal of Advances in Science, Engineering and Technology

Determination of Optical, Electrical, Structural, and Morphological Properties of $MAPbI_3$ Perovskite Films for Photovoltaic Applications

Silas Abok *, Elly Shatsala, Amos Nalianya, Francis Gaitho, Maxwell Mageto, Celline Awino

Department of Physics, Masinde Muliro University of Science and Technology, Kakamega, Kenya.

ABSTRACT

Perovskite devices based on methylammonium have been promising in the photovoltaic industry. A major challenge encountered with these devices lies in correlating their processing conditions, microstructure, and the overall photovoltaic performance. In particular, this paper addresses the challenge of accuracy in relating these properties by employing an automated SEM image Python segmentation approach that quantifies grain morphologies. The results derived from the segmentation technique assure reproducibility and bridge the gap between film fabrication, microstructure, and the properties. The resulting films were prepared by two-step spin coating and two-stage thermal annealing procedures, resulting in a planar inverted perovskite with architecture ITO/ PTAA/$MAPbI_3$/C_{60} /BCP/Ag. The fabricated films exhibit a tetragonal structure with high crystallinity, which is characterized by a conspicuous (110) plane. The results display fairly good homogeneity and large grain sizes averaging 212 nm, indicating a wide direct band gap of 1.52eV as displayed by the Tauc plots. The films show values of absorption coefficients exceeding 104 cm^{-1}. Generally, the resulting device has a high-power conversion efficiency of 13.91%, demonstrating that the automated SEM segmentation technique is a powerful tool useful in optimizing perovskite device processing parameters. Insights in this study, therefore, provide information on the enhancement of overall morphology-performance correlation leading to high-quality-film photovoltaic devices.

ARTICLE INFO

Keywords:
Automated SEM segmentation,
Bandgap,
$MAPbI_3$,
Morphology-performance correlation,
Perovskite devices.

Article History:
Received 8 September 2025
Received in revised form 26 October 2025
Accepted 11 November 2025
Available online 17 February 2026

1. Introduction

Perovskite devices based on methylammonium have been promising in the photovoltaic industry due to their strong absorption, ease of fabrication, band-gap tuning and low-temperature solution-based processing techniques as compared to their silicon counterparts (Min a., 2021; NREL, 2023). These noble traits advance the traditional solution-based based solar cell processing pioneered by dye-sensitized cells (Grätzel, 2003). Single-junction $MAPbI_3$ devices have achieved high power conversion efficiencies exceeding 25% and 34.6% in tandem configurations with enhanced material compositions, device architecture and interface engineering over the past few decades. (Zanatta, 2022; NREL, 2023). Among the various types of perovskite materials, $MAPbI_3$ possesses an optical bandgap in the range of 1.5 eV to 1.55 eV, strong absorption coefficients exceeding 104 cm-1, properties which are very crucial for effective light absorption capabilities over the ultraviolet - visible spectrum. (Mehri Ghasemi et al., 2025; Zhang et al., 2023). The material has always shown high crystallinity from XRD analysis and fairly large grain sizes of over 200 nm from SEM characterization (Castro-Méndez et al., 2019).

With all these developments in the perovskite technology, studies still show that there is overreliance on qualitative grain morphology, which is biased and rather time-consuming in nature. This leads to insufficient reproducibility, consumes time, and lacks systematic correlation (Saliba et al., 2016) with device performance since unbiased quantification of grain size and shape metrics still remains underexplored.

This study addresses this gap by introducing automatic Python-based SEM image segmentation, leveraging different modules to extract several hundred grains, and gives a high-throughput microstructural insight, introduces a buffer layer in the device to enhance stability, and correlates all these features to the device performance metrics. (Noman et al., 2024). This noble approach produced reproducible morphology-performance relations that offer an accurate

* Corresponding author. e-mail: aboksilas1996@gmail.com
Editor: Victor Odari, Masinde Muliro University of Science and Technology, Kenya.
Citation: Abok S., Shatsala M., Nalianya M., Gaitho F., Mageto M., & Awino C. (2026). Determination of Optical, Electrical, Structural, and Morphological Properties of $MAPbI_3$ Perovskite Films for Photovoltaic Applications. Journal of Advances in Science, Engineering and Technology 3(1), 11 – 25.

quantitative framework for optimizing perovskite film processing techniques, which improves on the overall device efficiency and stability, very crucial in designing more viable, stable, and scalable applications (Stranks, 2020).

2. Materials and Methods

2.1. Substrate Preparation

ITO-coated glass substrates (Biotin) measuring 20mm by 15mm with sheet resistance of 15Ω/sq were cleaned in soap water, acetone, distilled water, and finally in isopropanol (IPA, anhydrous, 99.8%, Sigma Aldrich) for 15 minutes each in a sonicator. The substrates were then dried under a nitrogen stream for 5 minutes and treated with UV ozone for 20 minutes to increase wetting of the surface and make it dust-free according to Panjan et al. (2022).

2.2. Perovskite Film Synthesis

A 1 Molar(M) of $MAPbI_3$ precursor solution was prepared by dissolving 158.97 mg MAI (99.99%, Sigma Aldrich) and 461.01mg PbI_2 (99.99%, TCI) precursor salts in a solvent mixture of Dimethyl formamide (DMF, anhydrous, 99.8%, Sigma Aldrich) of 6:1 v/v used as received without further purification. The precursor solution was stirred overnight using a magnetic stirrer to obtain a clear solution (Li et al., 2020). It was then filtered using a 0.22 µm thick polytetrafluoroethylene (PTFE) filter and spin-coated in two sequential steps: 1000 rpm for 15s followed by 5000 rpm for 25s. 60 µL of chlorobenzene (anhydrous, 99.5%, Sigma Aldrich) was then dripped onto the film 5 seconds before the end of spinning to evaporate the solvents and boost crystallization, as well as prevent moisture absorption. The resulting film was then annealed partially on a hot plate at 60 ^{0}C for 10 minutes and 100 ^{0}C for 15 minutes in a nitrogen-filled glovebox.

2.3. Perovskite Device Fabrication

A 5 mg/mL solution of poly [{bis (4-phenyl) (2,4,6-trimethylphenyl) amine] (PTAA, 99.99%, Sigma Aldrich) in chlorobenzene was set to spin on top of ITO coated glass substrate at 5000 rpm for 30 seconds to form a hole transport layer (HTM), this layer blocks surface traps (Pan et al., 2020). It was then annealed on a hot plate at 100 ^{0}C for 10 minutes to form a uniform film according to Traiwattanapong et al. (2024).

$MAPbI_3$ (214 nm) layer was deposited on top of the hole transport layer as described in section 2.2. It was then followed by evaporating a 20nm buckminster fullerene (C60, 99.99%, Sigma Aldrich) at high vacuum (~10-6 Torr) and spin-coated at 2000 rpm on top of the perovskite layer to form the electron transport layer (ETM). Approximately 7 nm bathocuproine (BCP, 99.99%, Sigma Aldrich) was thermally evaporated to form a buffer layer to prevent defects and improve charge movement to the top silver electrode (Sakomura et al., 2020). Finally, an 80 nm silver electrode was thermally evaporated to form the top contact, followed by UV-curable epoxy and a 2mm glass coverslip to provide mechanical protection to the device. The silver electrode forms a path for hole collection and creates ohmic links with the HTM (Cao et al., 2023).

2.4. Characterization Techniques

2.4.1. X-ray Diffraction (XRD)

The XRD technique was employed in the analysis of the crystal structure and phase purity assessment of the films. The XRD measurements were taken using a diffractometer with Cu $K\alpha$ radiation with $\lambda = 1.5406\text{Å}$ where diffraction patterns were recorded over a wide range of 10^0 to 60^0 with a continuous scan mode. The resulting XRD patterns were utilized in identifying crystallographic phases, determining the preferred orientation, and computing crystallite size and microstrain using Scherrer and Williamson-Hall methods.

2.4.2. Scanning Electron Microscopy (SEM)

This technique was used in investigating the surface morphology of the fabricated films. The SEM micrographs were scanned at an accelerating voltage of 5 -10 kV under high vacuum at different scale factors. The acquired images were then mapped on python environment for further segmentation via the watershed technique method after noise reduction using the thresholding method. Segmentation results displayed grain size distribution, number of detected grains, circularity, and solidity, as well as film thickness.

2.4.3. UV-Vis Spectroscopy

A commercial UV-Vis spectrophotometer was used to assess the optical properties of the fabricated films by measuring the absorbance and transmittance in a 40-900nm wavelength range. The measurements generated from this method yielded an absorption coefficient and optical bandgap estimated from Tauc plot analysis.

2.4.4. Current Density-Voltage (J-V)

J – V scanning was conducted in forward and reverse bias conditions under AM 1.5G solar illumination (100 mW/cm^2). These measurements revealed the photovoltaic performance parameters such as short circuit current density (J_{sc}), open circuit voltage (V_{oc}), fill factor (FF) and short-circuit current density (J_{sc}), open-circuit voltage (V_{oc}), fill factor (FF) and power conversion efficiency (PCE).

3. Results and Discussions

3.1. Structural Properties

The result in Fig. 1(a) shows the XRD pattern of the fabricated $MAPbI_3$ device, where the intensity (a.u) was plotted against diffraction angle (2θ). Dominant diffraction peaks were labelled in accordance to their respective Miller(hkl) indices such as (110), (211), (220), (310), (312) and (314), with the strongest peak evident at approximately 14.128°, corresponding to (110) plane, which is a unique identity of tetragonal perovskite phase $MAPbI_3$ at room temperature. The peaks at ~14° (110), 28° (220), and higher-order planes align with the tetragonal structure (space group 14/mcm) Niu et al. (2021). Similar indexed peaks have been observed elsewhere in the literature (Kumar et al., 2022), verifying the crystallographic identity and phase purity

of $MAPbI_3$ as supported by comparing the peaks with the JCPDS reference data.

The (110) orientation is very crucial for charge transport, as the Pb-I-Pb network along this direction enhances high carrier mobility (>20 $cm^2 V^{-1} s^{-1}$) (Tan et al., 2022), which is consistent with the high fill factor (63.8%) observed in this study. It is also instrumental in determining lattice characteristics of the film as it indicates a fairly larger interplanar spacing as compared with the higher -indexed planes, for instance, (220) or (310), allowing for more overlap between lead and iodide orbitals. This enhances charge delocalization and suppresses scattering. In addition, the wider lattice spacing gives room for a more open framework by reducing internal strain and defect formation, thereby leading to an improvement in crystallinity and low non-radiative recombination pathways (Guo & Jiang, 2024).

The results in Fig. 1(b) show an inverse proportionality between d-spacing and 2θ angles, and this clearly shows smaller interplanar distances at higher diffraction angles, consistent with Bragg's law. These findings are closely related to the results reported elsewhere in the literature (Pandey et al., 2021), which also relate a reduction in d-spacing values with a progressive increase in diffraction angles in perovskite materials.

Fig. 1(c) represents the correlation between d-spacing and the labeled Miller indices. As is evident, there was a progression from lower-order (110) planes toward higher-order indices such as (314), which is a progressive decrease in d-spacing, signifying tighter atomic packing in these crystallographic orientations. The notable decline in d-spacing from approximately 6.3 Å (110) to around 2.1 Å (314) confirms the crystal lattice planes' expected hierarchical ordering in the $MAPbI_3$ tetragonal crystal structure. Lower-index planes (110 & 211) have larger spacing reflecting fundamental lattice dimensions, while higher-index planes (310, 312, 314) have smaller spacing that reflects higher-angle planes with denser atomic arrangements. These findings are comparable with those reported elsewhere, which demonstrate decreasing lattice spacing with increasing Miller indices for $MAPbI_3$. For instance, Saliba et al. (2016) also confirmed the reported relation of Miller indices with lattice parameters in perovskite structures.

Fig. 1(d) shows the Full Width at Half Maximum (FWHM) of selected peaks ((110), (220), and (310)) plotted against Miller indices. The FWHM, which was measured in reciprocal space (Å-1), provides critical information on crystal quality, grain size, and strain. Smaller FWHM, such as at (110), indicates larger crystallite domains, lower lattice strain as well as better crystallinity, whilst larger FWHM at higher Miller indices (220, 310) is a suggestion of smaller crystallite sizes, increased lattice strain or even imperfections at higher-order reflections. The increasing trend of FWHM with higher Miller indices is attributed to reduced domain size or increased structural disorder at higher-order planes, and has an implication that the films are of greater sensitivity to micro strain at these crystallographic orientations.

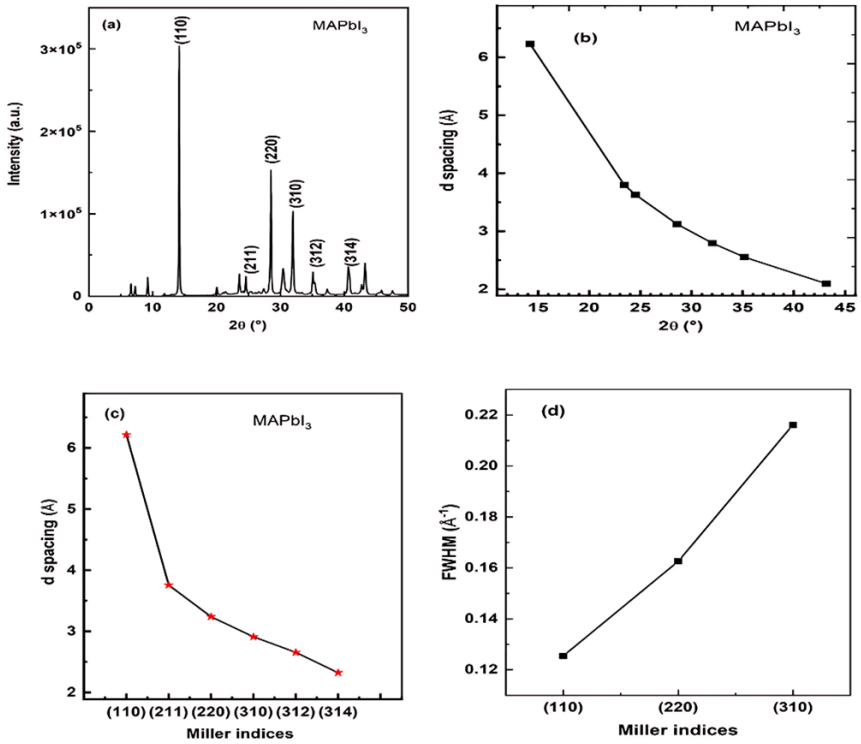

Fig. 1: X-ray Diffraction Pattern of $MAPbI_3$ (a), lattice spacing for $MAPbI_3$ (b), d-spacing for corresponding Miller indices (c), and FWHM vs three dominant Miller indices (d).

The experimentally observed peaks in this study were compared to the JCPDS reference data to ascertain the phase purity of the film. The observed peak positions align closely with the JCPDS (Table 1) reference data ($\Delta 2\theta \leq 0.15^0$), and this is a confirmation of the phase purity of the resulting perovskite films. However, there

is a relative deviation of the intensities from the reference values, particularly for the (211) reflection, which is weaker than expected. Generally, the gradual deviation signifies the presence of the preferred orientation rather than secondary phases, which is also strongly anchored by the formation of the tetragonal (110) reflection with a high crystallinity.

The crystallite sizes at different peak orientations (Table 2) were computed from the XRD peak broadening from the Full Width at half maximum (FWHM) by employing the Scherrer method, which is mathematically expressed by Eq. 1 below.

$$D = \frac{\kappa\lambda}{\beta cos\theta} \quad (1)$$

Where D is the crystallite size, κ is the shape factor, λ is the X-ray wavelength, β is the Full width at Half Maximum, and θ is the Bragg's angle.

The analysis of the (110), (211), (202), (310), (312), and (314) reflections yielded an average crystallite size of approximately 41±13 nm, as evident in Fig. 2, with a gradual decrease in crystallite size observed with increasing diffraction angle, which is very consistent with size-dependent broadening.

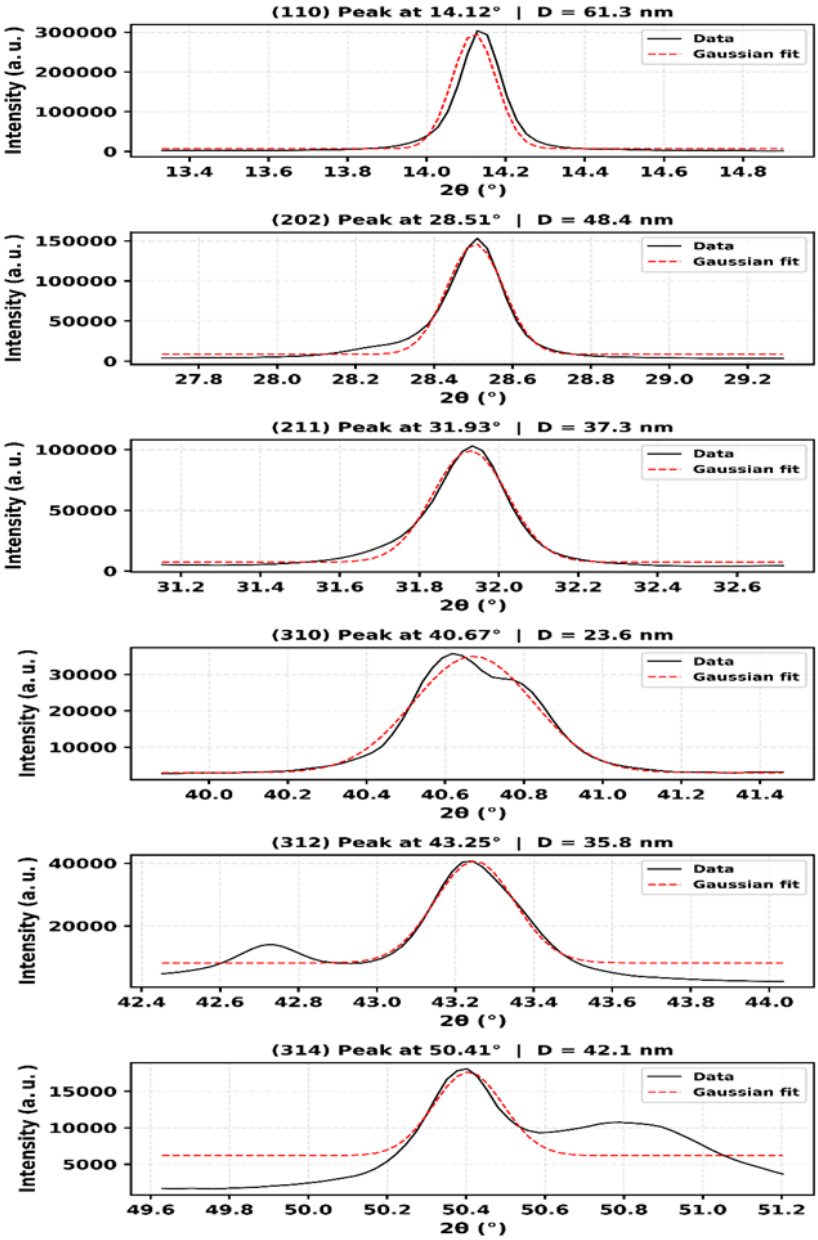

Fig. 2: Scherrer plots showing the variation of crystallite size with diffraction angle (2θ) for $MAPbI_3$ thin films derived from the Scherrer equation. The trend indicates a gradual decrease in crystallite size with increasing 2θ, consistent with size-dependent peak broadening.

The Scherrer method only accounts for the crystallite size and not micro-strain, as it assumes that peak broadening (Ulhakim et al., 2024) is dominated by finite crystallite size with a negligible contribution from lattice strain (Kim et al., 2019).

By employing the Williamson-Hall (W-H) method, expressed by Eq. 2 below.

$$\beta \cos\theta = \frac{\kappa\lambda}{D} + 4\varepsilon \sin\theta \quad (2)$$

Table 1: Comparison of the observed experimental peaks in this study and JCPDS (Card No. 96-451-8044) reference peak intensities for tetragonal $MAPbI_3$ (Cu Kα, λ = 1.5406 Å). Intensities are normalized to the (110) peak (100%). ΔI shows the deviation of observed intensity from the reference, highlighting preferred orientation effects.

Miller indices(hkl)	2θ (Reference, °)	Reference intensity, (I ref) (%)	Observed 2θ values	Observed intensity (I obs) (%)	Δ2θ (°)	ΔI(%)
(110)	14.10	100	14.12	100.0	+0.02	0.0
(211)	23.50	40	23.54	8.8	+0.04	-31.2
(220)	28.40	55	28.51	50.4	+0.11	-4.6
(310)	31.90	30	31.93	33.9	+0.03	+3.9
(312)	40.50	20	40.62	11.8	+0.12	-8.2
(314)	43.10	15	43.24	13.4	+0.14	-1.6

Table 2: Crystallite sizes for different peak orientations at different Full Width at Half Maximum (FWHM) values computed from the Scherrer method

Miller indices (hkl)	2θ (°)	FWHM (°)	FWHM (rad)	θ (rad)	Crystallite Size (nm)
(110)	14.12	0.130	0.00227	0.1234	61.3
(202)	28.50	0.169	0.00295	0.2488	48.4
(211)	31.93	0.221	0.00386	0.2787	37.3
(310)	40.67	0.359	0.00627	0.3550	23.6
(312)	43.25	0.239	0.00417	0.3775	35.8
(314)	50.41	0.208	0.00363	0.4399	42.1

Where ß denotes Full Width at half Maximum of the peak (FWHM), θ, the Bragg's angle, κ the shape factor (0.9), λ X-ray wavelength, D the crystallite size and ε is the micro strain in the crystallite, the crystallite size was interpreted as the y-intercept given by κλ/D and Micro-strain derived from the slope of the graph (ε), the crystallite size and micro-strain were estimated by this method since it accounts for strain broadening. This resulted into crystallite size of 78.21 nm (Fig. 3c) and micro-strain of 3.936×10^{-4} (0.0394%) from linear regression fit.

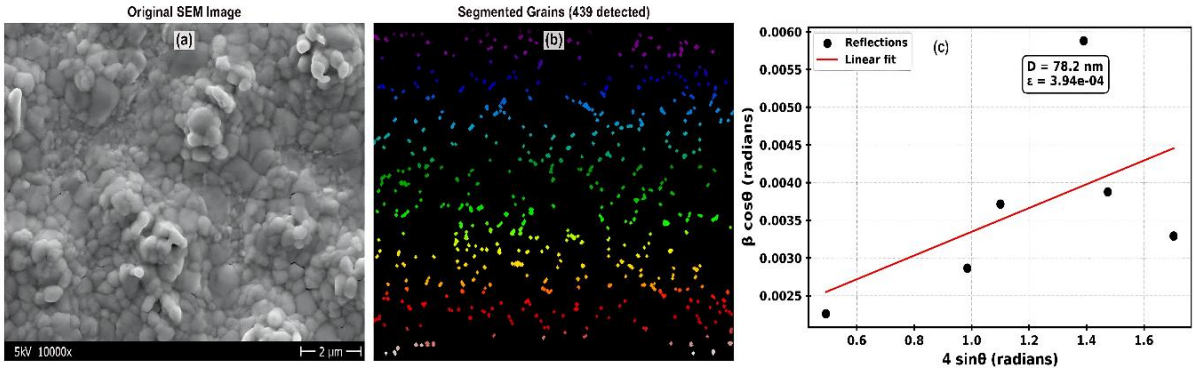

Fig. 3: Top View of the original SEM micrograph of $MAPbI_3$ at 10,000X scale factor (a) and corresponding segmented SEM image depicting grain boundaries with 439 detected grains and distinct crystallite regions(b) Williamson- Hall analysis for $MAPbI_3$ films with linear fit (R^2=0.2965) to determine Crystallite size and Micro-strain; the slope represents strain (ε), whilst intercept corresponds to crystallite size (D)(c).

The value of the crystallite size obtained from the W-H approach was bigger as compared to Scherrer method because the method accounts for strain broadening (Williamson et al., 1953), which is not considered in the Scherrer method. The low micro-strain value, which is typically less than 0.1 %, is an indication of good crystalline quality with minimal lattice distortions (Rahman & Edvinsson et al., 2020). The long deposition time (10 mins) and annealing temperature (100^0C) generally enhance crystallinity by promoting grain growth, resulting in larger crystallite sizes and reduced microstrain (Yu et al., 2022) due to improved atomic ordering and stress relaxation. Conversely, higher spinning speeds tend to yield thinner films with finer grains and elevated microstrain, as rapid solvent evaporation limits crystal growth and induces lattice distortions. These results, in general, suggest a nanocrystalline film with relatively small crystallites and excellent perfection (Zhang et al., 2022), which are consisted with previously reported $MAPbI_3$ thin films of comparable preparation conditions.

3.2. Morphological Analysis

Fig. 3(a) shows a SEM micrograph of polycrystalline $MAPbI_3$ scanned at a scale factor of 10,000X at an accelerating voltage of 5kV. In Fig. 3(b), the image is segmented, and a total of 439 grains were detected. The size distribution histogram with a bin width of 8.5 nm indicates that the film has a mean diameter of 205±47 nm (Fig. 4a), which is an indication of a non-nucleation-dominated growth due to the optimized annealing temperature, and a slightly bimodal distribution suggested by a large standard deviation (±47 nm). Since the grains are of favorable size (>200 nm), it implies that there is low grain boundary density that may reduce non-radiative recombination and therefore, improve charge transport, but may slightly reduce film coverage as film thickness of 100-300 nm is known to be ideal for solar cells (An et al., 2021).

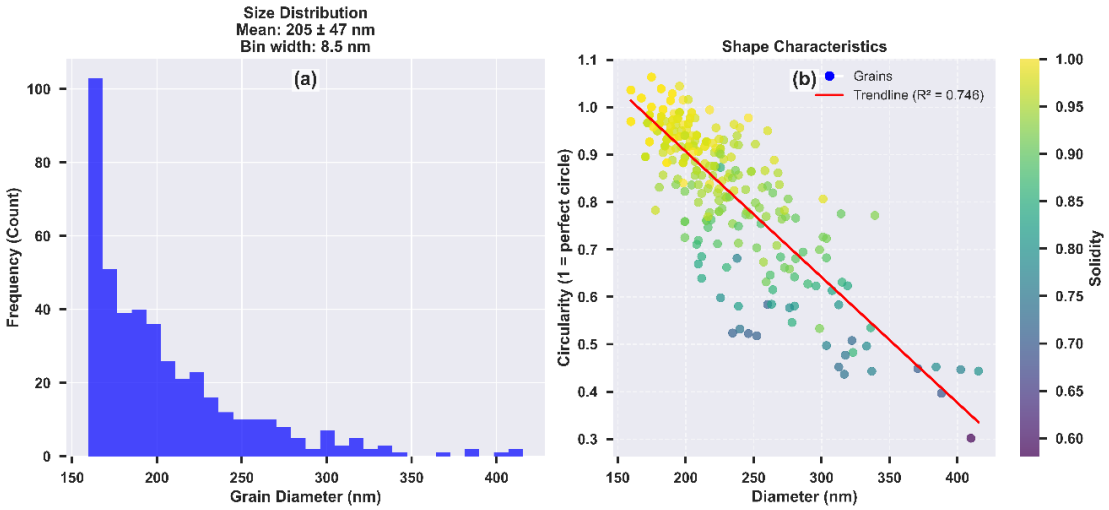

Fig. 4: Grain Size distribution histogram showing mean, standard deviation, and bin width of 8.5 nm (a) and Shape characteristics plots with blue dots denoting grains and red trendline showing linear correlation (b)

The annealing profile also played a significant role, as the exposure time of 10 minutes at annealing temperatures of 100°C provided enough time for grain boundaries to merge effectively. The aspect ratio data shown in Fig. 4(b) (1.1 to 0.3 circularity) reveal dominant equiaxed grains (1.0 - 1.1) as most of the grains are crowded in this region, resulting in isotropic crystal growth (Nie et al, 2015) during the 100°C annealing temperature. This is an indication of nearly perfect grains, which offer a very efficient surface for sunlight absorption, thus enhancing the device performance. The presence of some irregular grains (0.3- 0.5) was likely due to incomplete coalescence during spin-coating and local stoichiometry variations, such as PbI_2-rich domains; thus, more time should be allowed for the complete coalescence during annealing.

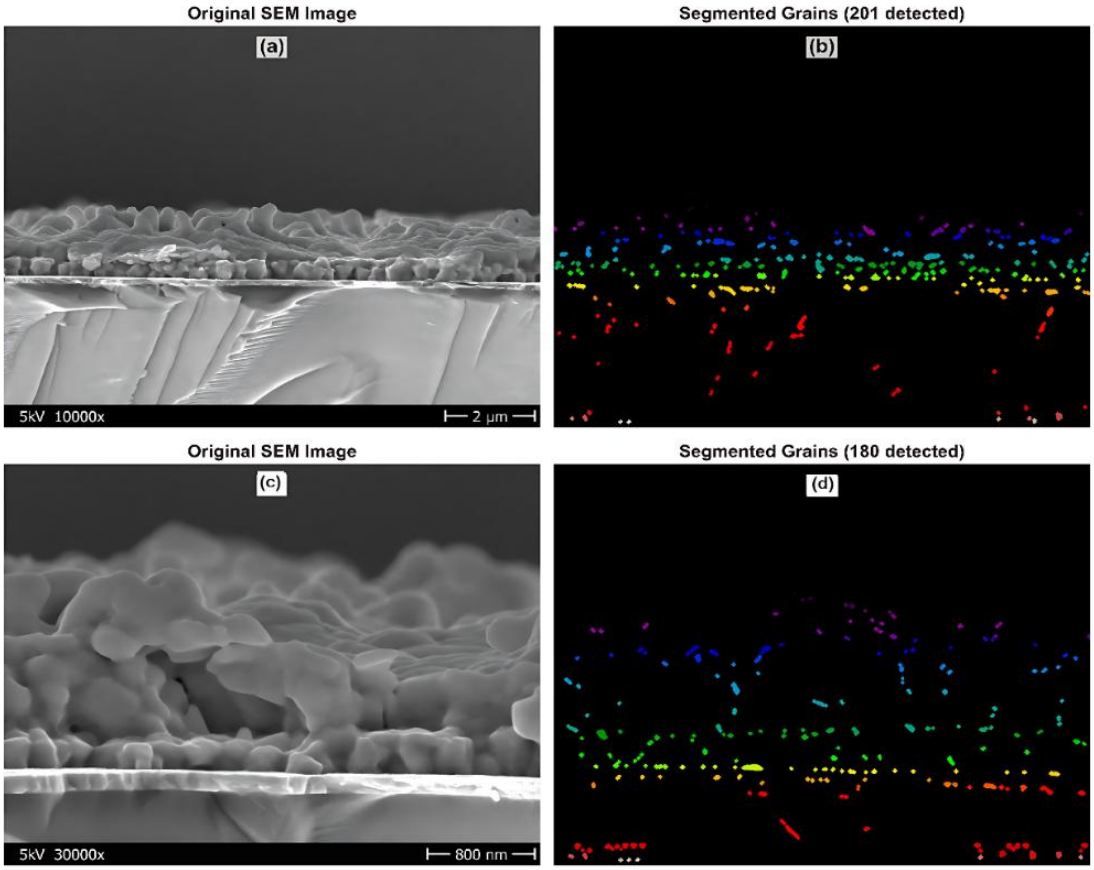

Fig. 5: Cross-sectional view of the original SEM micrograph at 10,000X (a) and 30,000X scale factor (c), and Corresponding SEM image segmentation with 201 (b) and 180 (d) detected grains showing grain boundaries and distinct crystallite regions.

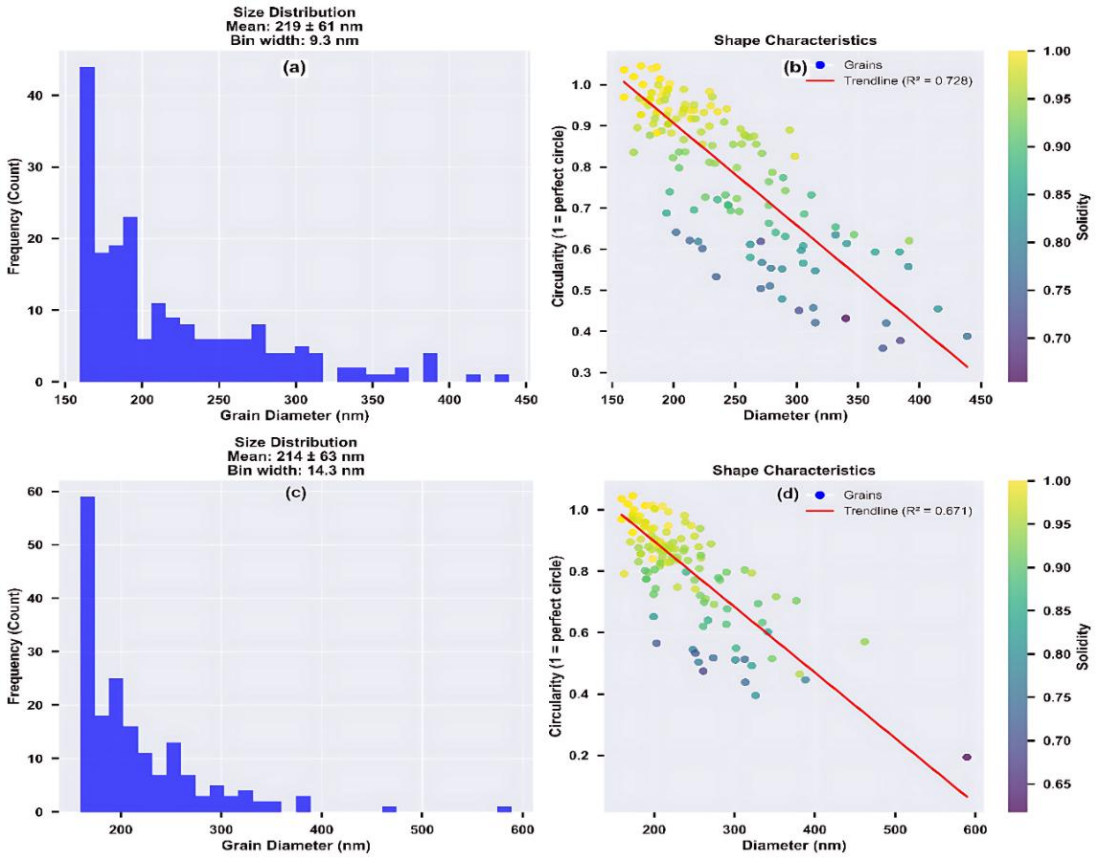

Fig. 6: Grain Size distribution histogram showing mean, standard deviation, and bin widths (a) &(c) and Shape characteristics plots with blue dots denoting grains and red trendline showing linear correlation (b)&(d)

In Fig. 5(a), the SEM image was scanned at a scale factor of 10,000X and depicts a dense and continuous film with a relatively uniform distribution of grains. From automatic image segmentation in Python, a total of 201 grains were identified (Fig. 5b). The resulting size distribution histogram in Fig. 6(a) shows that the average grain thickness is 219 ± 61 nm, with most grains falling within the 150-300 nm range. This range is considered optimal for planar inverted architecture since it is known to balance strong light absorption and efficient carrier diffusion. Very small grain sizes below 100nm experience a high density of grain boundaries, which result in increased trap - assisted recombination (Li et al., 2025), whilst excessively large grain sizes more than 500 nm result in non-uniform film coverage and reduced interfacial contact (Liu et al., 2023). In this study, the results lie within the ideal range for minimized recombination and optimized charge transport.

Fig. 6(b) shows grain shape characteristics, including circularity and solidity, where most grains exhibited circularity values close to 1.0 and high solidity, demonstrating a well-defined, compact morphology with minimal edge roughness. These metrics reflect high crystalline quality and low morphological disorder, which are normally associated with enhanced open-circuit voltage (V_{oc}) and fill factor (FF) (Shaik *et al.*, 2023).

A noticeable decrease in circularity and solidity was observed in grains exceeding 300 nm in diameter, and this suggests a minor aggregation or incomplete crystal boundaries, which is very common in films without controlled crystallization steps (Wanyonyi *et al.*, 2024). Cross-sectional scanning electron microscopy (SEM) imaging at a magnification of 30,000X in Fig. 5(c) was conducted to quantify the grain structure of the methylammonium lead iodide ($MAPbI_3$) perovskite film. Through automatic image segmentation and analysis shown in Fig. 5(d), a total of 180 distinct grains were detected. These grains yielded a mean grain size of 214 ± 63 nm, indicating a moderately uniform crystalline structure.

The histogram of the grain size distribution in Fig. 6(a) revealed that most grains were concentrated within the 150-250 nm range, and this is a suggestion of a narrow dispersion with limited presence of either very small or exceptionally large grains. Specifically, the size distribution representation exhibited a peak around 200 nm, and this signifies a prevalence of intermediate-sized grains. The depicted uniformity in grain size is very crucial as it reduces grain boundary density and hence minimizes charge carrier recombination and enhances carrier diffusion lengths (Kumar *et al.*, 2022).

The shape characteristics in the scatter plot (Fig. 6d) showed a significant proportion of the grains falling within a near-spherical to sub-rounded geometry. This indication is very advantageous in achieving dense film packing and enhanced film continuity. These results indicate high crystallinity with a positive impact on light harvesting and charge transport by the perovskite layer (Choi *et al.*, 2020)

3.3. Optical Properties

3.3.1. The Reflection, Absorption, and Transmission Spectra

Fig. 7(a) shows plots of Transmittance (%T), Reflectance (%R), and Absorbance (%A) spectra of the fabricated perovskite material. In the reflection spectrum, the reflectance remains nearly zero between 400nm and 600 nm, with the minimum occurring around 700nm, showing that the material absorbs the major part of the incident light within the visible range and has minimal optical losses that may result from reflection. This strong light absorption coincides with the photon energies beyond the band gap (~1.52 eV) of the material. The notable small rise in reflectance for the values above 700 nm is attributed to the effects of optical interference or the onset of low absorption as the photon energy reduces below the bandgap.

The blue curve (A) shows a strong absorption between 400nm and 750nm. However, there is a notable sharp decline in absorption beyond 760 nm, and this marks the band-edge of the material. This is a unique behavior of $MAPbI_3$ - based perovskites since they possess strong light-harvesting capability in the visible regime due to their direct band gap nature. The sharp absorption onset is an indication of high crystallinity and reduced defect- induced sub-bandgap states.

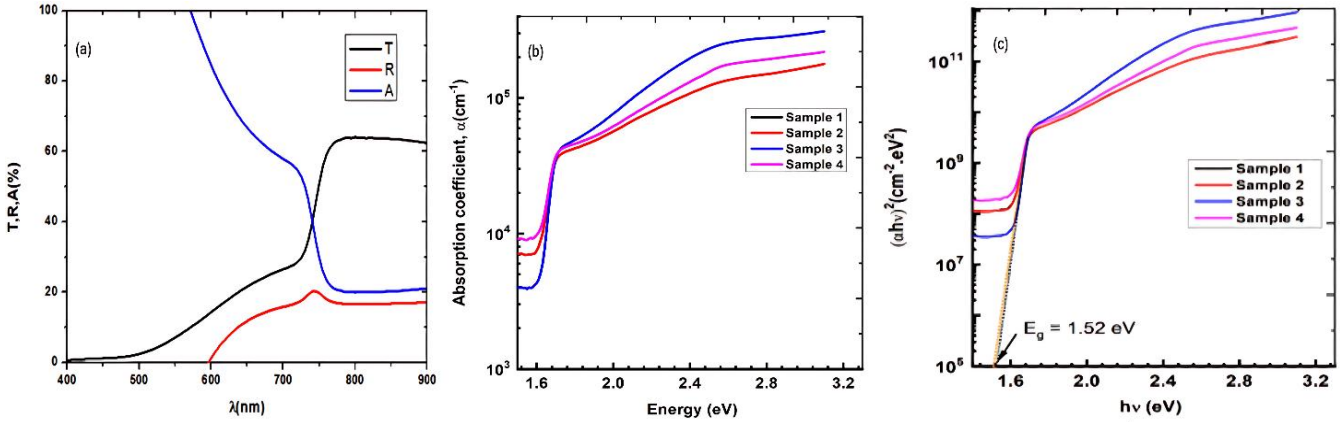

Fig. 7: Reflection, Absorption, and Transmission spectra (plots of TRA; black, red, and blue curves respectively) (a), Absorption coefficient vs Photon energy for the different Samples (b), and Tauc plot for $MAPbI_3$ indicating the extrapolated bandgap of the fabricated absorber (c).

The black curve (T) indicates that there is a persistent low transmission in the visible regime at high absorbance, indicating efficient light harvesting. Notably, there is a gradual increase in transmission beyond 750nm, and this corresponds to wavelengths with photon energies below the bandgap in the regions where the material becomes more transparent. The property is important since, while the material absorbs sufficient light in the visible to near infrared regions, it also permits transmission for longer wavelengths, reducing thermal losses and enhancing the overall photovoltaic performance.

This overall analysis of reflectance (R), absorbance (A), and transmittance (T) spectra reveals the material's strong potential as an absorber component in next-generation solar photovoltaic modules. The peaks identified in the UV-Vis spectrum correlate with electronic transitions within the $MAPbI_3$ thin film and hence, offer very important insights into its optical properties and electronic structure.

3.3.2. UV-Vis Absorption Edge Analysis

Fig. 7(b) displays the absorption coefficient (α) as a function of photon energy for four samples. All the samples show a pronounced increase in absorption near 1.6 eV, which is a unique characteristic of a direct bandgap semiconductor. The absorption onset observed was in close agreement with previous reported data on methylammonium lead iodide ($MAPbI_3$), which typically showed a band gap energy in the range of 1.515 to 1.65 eV (Noh et al., 2013; Xing et al., 2013).

The absorption coefficient for all the samples exceeded 104 cm-1 at energies above 1.6 eV. This high absorption coefficient value was a defining feature of hybrid halide perovskites and indicates the material's capability to absorb most of the incident visible light within a very short wavelength. The strong absorption was mainly due to the high oscillator strength of electronic transitions involving the lead (Pb) 6p and iodine (I) 5p orbitals, as well as the influence of spin-orbit coupling in the conduction band (Sahare et al., 2025).

Comparing the four samples, it is evident that sample 3 has the highest absorption in the energy regions, indicating that the films are of superior quality, a property that can be attributed to larger grain sizes, enhanced crystallinity, and reduced trap-assisted density. The higher absorption in the sample agrees well with the results reported elsewhere in the literature (Jeon et al., 2014), which indicate that superior film morphology promotes light harvesting due to low scattering losses and defects.

On the other hand, sample 2 indicates the lowest absorption; this may be due to poor film morphology, incomplete surface coverage, or increased defect concentrations, which may lead to more pronounced sub-gap absorption or non- radiative recombination. Reports from literature (Das Adhikari et al., 2025) argue that $MAPbI_3$ films with incomplete surface coverage or pinholes show reduced absorption and photovoltaic

performance as a result of back reflection and parasitic absorption, as supported elsewhere (Tonui et al., 2018).

The progressive increase in the absorption coefficient above the band edge is normal for direct band gap materials and indicates the quality of the transitions. The spectral features of all the samples also confirm the absence of significant secondary phases (Hansen, 2023) like PbI_2, which would have manifested as additional absorption peaks around 2.4 eV.

The absorption behavior of all four samples confirms that $MAPbI_3$ possesses an ideal band structure for solar energy conversion. The large absorption coefficients and direct bandgap make $MAPbI_3$ (Subha et al., 2023) suitable for ultrathin absorber layers that allow for the fabrication of high-efficiency solar cells with thicknesses below 500 nm. The variation in absorption among the samples in this study underlines the importance of precise control over film deposition parameters such as solvent composition, precursor ratio (MAI: PbI_2), spin-coating speed, as well as annealing temperature (Saliba et al., 2016).

The optical band gap of the fabricated perovskite thin films was determined using the Tauc method, based on the absorption coefficient (α) extracted from UV-Vis transmission and Reflection data. Complementary methods such as modulated surface photovoltage (M-SPV) have been used extensively in validating the onset of band gap and sub-gap transitions, reports elsewhere in the literature (Omondi, 2018). Tauc analysis from plots of $(\alpha h\upsilon)^2$ versus energy of photons($h\upsilon$) was extracted for all the samples, as evident in Fig. 7(c), where a linear fit of the near-absorption edge on the energy axis gave an estimation of bandgap values within a narrow range of 1.51 eV to 1.52 eV, with an average of 1.52 eV. The obtained bandgap satisfied the known range of bandgap of $MAPbI_3$, which has been reported elsewhere in the literature to fall within the 1.50 – 1.55 eV range (Kojima et al., 2009; Subha et al., 2023).

The small deviation between the absorption onset at 1.6 eV and the Tau-derived bandgap of 1.52 eV basically shows that there is a sharp increase in absorption, a value usually smeared by Urbach tails due to sub-bandgap states (De Wolf et al., 2014). Additionally, the Tauc method is an extrapolation that represents the immediate band-to-band transition. Excitonic effects between 10 -50 meV binding energies may also appear at the absorption edge, making activation slightly higher than the actual bandgap (Even et al., 2014). Absorption offset of 50 meV – 100 meV is typical in high quality $MAPbI_3$ films (Mehri Ghasemi et al., 2025; Green et al., 2022). Thus, the difference of approximately 0.08 eV observed in this study is consistent with the intrinsic optical behavior of perovskites and can be attributed to excitonic absorption, slight crystallite size differences, local film thickness variations, and tail-state distribution, but not error in the measurements, as it may be due to minor stoichiometric imbalances during spin-coating. The resulting bandgap value of 1.52eV falls within the Shockley-Queisser limit for single junction solar cells (1.34- 1.5 eV), suiting $MAPbI_3$ for photovoltaic applications. (Shao & Loi, 2021; Soltani et al., 2025). The slightly lower bandgap of $MAPbI_3$ enables it to capture a broad portion of the solar spectrum from Ultraviolet to near-infrared regions as compared to wider band gap counterparts such as $MAPbI_3$, ranging from 2.2 eV to 3.0 eV, hence, a favorable candidate for enhancing photocurrent generation (Shao & Loi, 2021; Soltani et al., 2025).

3.4. Electrical properties

Fig. 8 shows J – V characteristics and the photovoltaic performance metrics of the resulting perovskite device, scanned in the forward and reverse bias conditions to evaluate hysteresis effects, frequent in single-cation perovskite devices. Subsequent scanning in both forward and reverse directions yielded -23.33 mA/cm^2 and -23.36 mA/cm^2 for short circuit current densities, respectively. The negative sign is an indication of power withdrawal from the device during testing.

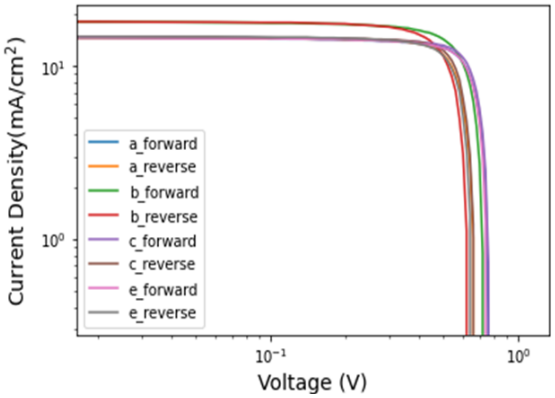

Fig. 8: J-V Characteristic curves for both forward and reverse conditions.

Recent optimized studies have been used to contextualize the resulting PCE of 13.9% with V_{oc} = 0.93 V, J_{sc} = 20.7 mA/cm^2, and FF = 63.8% for an average grain size of 212 ±54 nm in Table 3. Based on $MAPbI_3$, Tipparak et al. (2025) reported a quantum-dot passivated device with a V_{oc} of 1.08 V, J_{sc} of 20.7 mA/cm^2, FF = 72.6 %, and PCE of 16.1 % for grain sizes in the 200 – 400nm range. Additionally, Kim et al. (2023) reported V_{oc} = 1.21 V, J_{sc} = 21.2 mA/cm^2, FF =

The device yielded an open circuit voltage (Voc) of 0.9338V and 0.8985 V for forward and reverse bias conditions, respectively. Theoretically, the values are lower than the limit for $MAPbI_3$ (~1.2 V), and this may be due to some levels of non-radiative recombination resulting from interface defects or mobile ion accumulation at interfaces, a known issue in perovskites (Chen et al., 2023). However, experimental results from previous studies show Voc values ranging from 0.9 V to 1.05 V, aligning well with this study (Kumar & Ranjan, 2021). The device yielded a maximum power point voltage (P_{max}) of 13.91 mW/cm^2 and 12.25 mW/cm^2 under forward and reverse bias conditions, respectively. under forward and reverse bias, respectively, and voltage at maximum power point (V_{mpp}) of 0.68 V and 0.66 V in forward and reverse scans, respectively, a further demonstration of the impact of scan direction on

performance parameters of the device. The fill factor (FF) was found to be 63.83% under forward bias (Fig. 9) forward bias and 58.35% under reverse bias, indicating a moderate level of hysteresis, a common trait in high-efficiency $MAPbI_3$ cells, often achieving FF values in the range of 70-80% (Kim et al., 2023). However, slightly lower, the obtained FF in this study still falls within the range reported in perovskite devices without advanced interface engineering or additive passivation. The reduced FF in the reverse scan direction was initiated with capacitive and ionic effects within the perovskite layer, which perturb charge collection dynamics (Filipoiu et al., 2022).

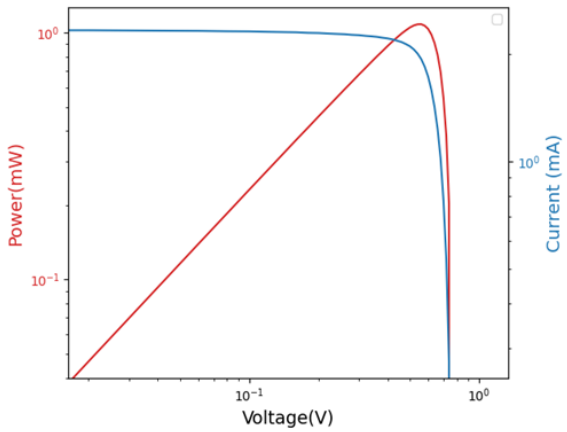

Fig. 9: Fill factor and efficiency for the resulting device

The overall power conversion of the device is recorded at 13.91% and 12.25% for forward and reverse scans, respectively. These results are in agreement with the early $MAPbI_3$-based devices with PCEs of 12 – 15% reported elsewhere (Kojima et al., 2009) but fall short of the state-of-the-art >20% efficiencies, attainable via compositional engineering and interface modification (Jagadamma & Wang, 2021). The declining PCE in reverse scan shifts the focus on the impact of hysteresis, indicating the need for further optimization.

As evident from Fig. 10 (a) and Fig. 10 (b), the series and shunt resistances were analyzed from the J- V curves, resulting in a higher fill factor for low values of series resistance and higher fill factors for high values of shunt resistance. For instance, in Fig. 10 (a), the FF is higher (61.2%) at a shunt resistance (Rsh) of 0.72Ω.cm^2 and lower (59%) at 0.61 Ω.cm^2. At higher shunt resistance, leakage currents fall, limiting recombination and saving on open circuit voltage, while maintaining the fill factor of the device (Kumar & Ranjan, 2021). In Fig. 10(b), there is a clear indication that rising Rs lowers FF, for example, as the series resistance (Rs) increases from 0 Ω.cm^2 to 0.6 Ω.cm^2, the FF is subjected to a fall from 61.2% to 59.0%. This is a result of the losses that occur when charges move through each device layer and contact. A sufficient drop in series resistance impedes current near the maximum power point, making the FF and device efficiency lower (Jeon et al., 2014). To enhance perovskite devices, it is vital to simplify the electronic states. In this study, silver nanowires in the electrodes lower the series resistance (Tan et al., 2020) by enhancing FF by about 5 %, crucial in larger devices where the issue of lateral resistor losses matters the most (Tan et al., 2022). This result agrees well with previous studies showing that Rsh helps ensure that devices operate smoothly and reliably. For example, Wu et al. (2024) found that controlling the interface to eliminate defects raised both R_{sh} and FF values, as high Rsh is necessary for perovskite solar cells since a defect or hole formed during film deposition can be a big problem in the long run.

Table 3: Comparative Analysis of $MAPbI_3$-Based Perovskite Solar Cell Performance

Study & Journal	Year	Architecture / Key Innovation	E_g (eV)	Grain Size (nm)	V_{oc} (V)	J_{sc} (mA/cm^2)	FF (%)	PCE (%)
This Work	**2025**	**ITO/PTAA/$MAPbI_3$/C_{60}/BCP/Ag** Inverted (p-i-n); **Automated Python SEM analysis**	**1.52**	**212 ± 54**	**0.93**	**23.3**	**63.8**	**13.9**
$MAPbI_3$ PSCs-Aging Treatment (Chem. Eng. J.)	2023	Aging Treatment Two-step deposition; 60-day aging improves FF	1.57	~300-500	1.21	21.5	80.8	21.1
$MAPbI_3$ QDs-CsFA PSCs (ACS Appl. Energy Mater).	2025	$MAPbI_3$ QDs on CsFA Perovskite QDs as a passivation layer	1.56	200-400	1.08	20.7	72.6	16.1

The low series resistance from the fabricated device is an indication of sufficient charge collection and reduced overall resistance in the device, attributed to the hole transport layers (PTAA), which allow for good hole mobility, better contact of holes with the perovskite, and reduced resistive losses (Guo et al., 2021). The key reason for the imbalance of shunt resistance is either the presence of thin film cavities or the migration of ions, which may lead to mild hysteresis and temporary variations in the device operation (Gao et al., 2022; Er-raji et al., 2024). The comparable difference between forward and reverse scan metrics indicates the presence of some hysteretic levels, a normal issue due to ion migration, interfacial charge accumulation, and trap states, yet to be addressed fully in $MAPbI_3$ (Unger et al., 2014). The fill factor and Voc were particularly affected, and while the Jsc remains consistent, the overall PCE shows a drop of about 2% in the reverse scan. This is in line with reports by Chen et al. (2023), who emphasized the role of slow-moving ionic species in enhancing internal electric fields, affecting the J-V curve depending on scan direction.

A number of strategies, such as the use of mixed cations of MA/FA/Cs, inclusion of passivation additives such as KI, C4H12N, and introducing more stable transport layers such as NiO_x, PCBM, have been put in place to suppress hysteresis and improve stability as

reported elsewhere in the literature (Sivakumar et al., 2023). Such strategies could increase the FF beyond 75 % and raise efficiencies towards the 18 -21% range for $MAPbI_3$-based devices.

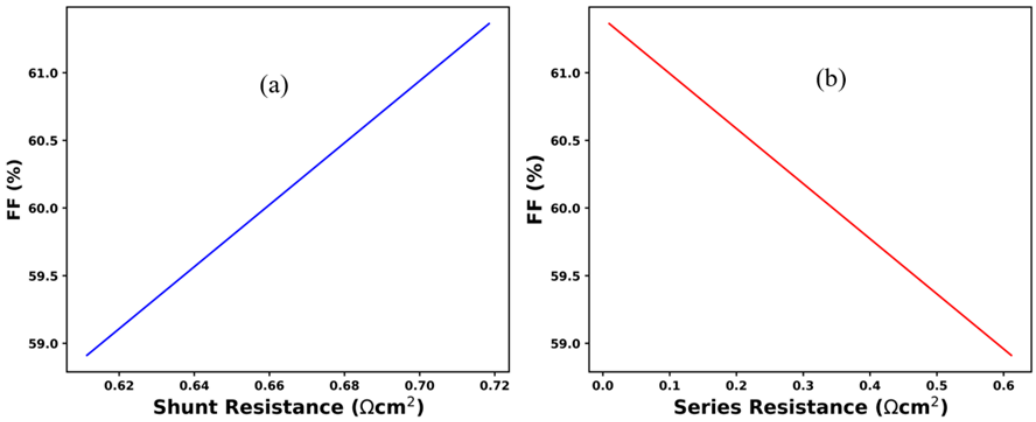

Fig. 10: *(a) Variation of FF with Shunt Resistance (R_{sh}); (b) Variation of FF with Series Resistance (R_s).*

The bar chart in Fig. 11 shows a typical power conversion efficiency (PCEs) for four perovskite solar cell samples, under both forward and reverse scans. From the results, it is clear that there is a variation in performance metrics based on the direction of scanning. For example, sample 1 has a PCE of 13.4% in reverse bias, and when forward biased, PCE rises to 13.7%. Sample 2 demonstrates a comparable trend at 12.2% when reversed and 13.9% when followed forward. In the reverse bias condition, acceleration of PCE is higher in sample 3 (11.5%) as compared to the forward bias, with a value of 10.3%.

Sample 4 shows an identical trend with the reverse scan performing slightly better (11.4%) than the forward (11.2%) scan. This is a suggestion of ferroelectric effects; ion migration and charge build up that occur at the perovskite layer (in agreement with Lyu & Park, 2020). PTAA, as a hole transport material, shows less hysteresis than TiO_2 due to its smooth energy alignment and fewer traps (Min et al., 2021; Wei et al., 2023). Significantly, there was not much difference detected between reverse and forward scans in all the samples, implying that the device structure is stable under transient ionic actions and likely to be reliable over time.

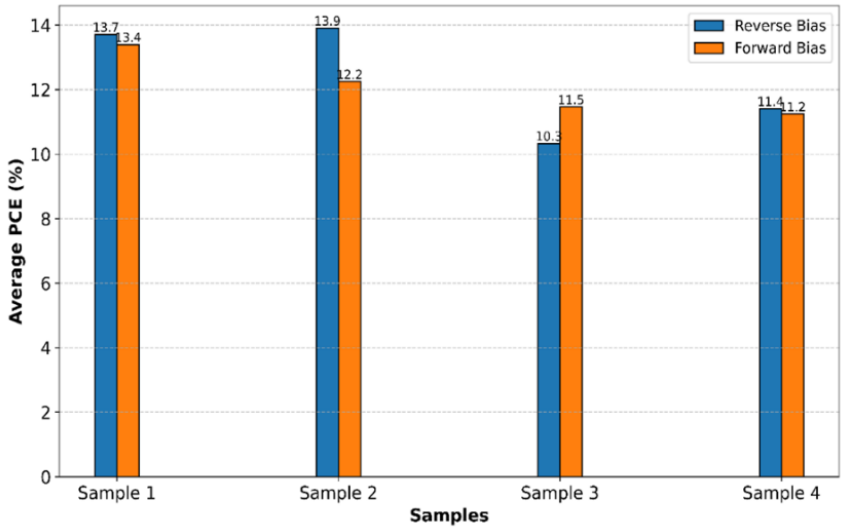

Fig. 11: Average power conversion efficiencies for different samples of the fabricated device.

The overall hysteresis evident in the J-V scans suggests that ion migration and interfacial defects remain significant, as it limits further limit the device stability and performance. Trap states and defect-induced recombination pathways under illumination have been quantified in recent studies via MSPS, indicating a reduction in transport length within 12 hours of light soaking as reported elsewhere (Awino et al., 2020). These prominent issues can be addressed through more advanced interface engineering, surface passivation, and grain growth strategies, which offer a clearer pathway to bridge the efficiency gap toward state-of-the-art $MAPbI_3$ devices and meet the long-term reliability standards required for commercial viability (Sakhatskyi et al., 2022)

4. Conclusions

In this study, the properties of the fabricated films were analyzed comprehensively by correlating them with the overall photovoltaic metrics of the resulting planar inverted device. The fabricated films exhibit a tetragonal structure with high crystallinity, which is

characterized by a conspicuous (110) plane. The results display fairly good homogeneity and large grain sizes averaging 212 nm, indicating a wide direct band gap of 1.52eV as displayed by the Tauc plots. The films show values of absorption coefficients exceeding 10^4 cm^{-1}, average crystallite size of 41nm, as well as low microstrain of 3.936×10^{-4} derived from Williamson- hall analysis, indicating excellent crystalline quality with low lattice distortions. Generally, the resulting device has a high power conversion efficiency of 13.91%, demonstrating that the automated Python segmentation technique is a powerful tool useful in optimizing perovskite device processing parameters.

From the results in this study, we propose the implementation of defect passivation and interface engineering, such as self-assembled monolayers at HTM, and the introduction of a Lewis base in the precursor to raise Voc and FF by suppressing non-radiative recombination for better results. Secondly, compositional and morphological optimization should be used to substitute MA^+ with FA^+/Cs^+ mixtures for improved stability and control of the bandgap. Future work should make use of solvent vapor annealing or volatile crystallization guides to facilitate the growth of larger and more uniform grains, guided by the automated Python SEM image segmentation. Finally, more advanced characterization techniques such as time-resolved photoluminescence and EIS should be implemented for accurate quantification of recombination and ion migration. These improvements can further be validated through accelerated stability tests and industrial-scale deposition techniques such as blade and slot-die coating to address the key challenges outlined for commercial viability.

Acknowledgments

The authors would wish to acknowledge the Department of Physics, Masinde Muliro University of Science and Technology (MMUST) for providing laboratory facilities that played an instrumental role in the experimental work. We also extend our appreciation to the World Academy of Sciences (TWAS) for donating the glovebox equipment, which played a pivotal role in the synthesis of the perovskite films.

References

An, Q., Paulus, F., Becker-Koch, D., Cho, C., Sun, Q., Weu, A., Bitton, S., Tessler, N., & Vaynzof, Y. (2021). Small grains as recombination hot spots in perovskite solar cells. Matter, 4(5), 1683-1701. https://doi.org/10.1016/j.matt.2021.02.020.

Awino, C., Barasa, G., & Odari, V. (2020). Light induced degradation of the transport length of CH3NH3PbI3 studied by modulated surface photovoltage spectroscopy after Goodman. Organic Electronics, 77, 105503. https://doi.org/10.1016/j.orgel.2019.105503.

Cao, M., Ji, W., Chao, C., Li, J., Dai, F., & Fan, X. (2023). Recent advances in UV-cured encapsulation for stable and durable perovskite solar cell devices. Polymers, 15(19), 3911. https://doi.org/10.3390/polym15193911.

Castro-Méndez, A., Hidalgo, J., & Correa-Baena, J. (2019). The role of grain boundaries in perovskite solar cells. Advanced Energy Materials, 9(38). https://doi.org/10.1002/aenm.201901489.

Chen, X., Geng, C., Yu, X., Feng, Y., Liang, C., Peng, Y., & Cheng, Y. (2023). Additive engineering in spray enables efficient methylammonium-free wide-bandgap perovskite solar cells. https://doi.org/10.2139/ssrn.4386008.

Choi, K., Choi, H., Min, J., Kim, T., Kim, D., Son, S. Y., Kim, G., Choi, J., & Park, T. (2020). A short review on interface engineering of perovskite solar cells: A self-assembled monolayer and its roles. Solar RRL, 4(2). https://doi.org/10.1002/solr.202070021.

Das Adhikari, R., Patel, M. J., Baishya, H., Yadav, D., Kalita, M., Alam, M., & Iyer, P. K. (2025). Decoding recombination dynamics in perovskite solar cells: An in-depth critical review. Chemical Society Reviews, 54(8), 3962-4034. https://doi.org/10.1039/d4cs01231c.

De Wolf, S., Holovsky, J., Moon, S., Löper, P., Niesen, B., Ledinsky, M., Haug, F., Yum, J., & Ballif, C. (2014). Organometallic halide perovskites: Sharp optical absorption edge and its relation to photovoltaic performance. The Journal of Physical Chemistry Letters, 5(6), 1035-1039. https://doi.org/10.1021/jz500279b.

Er-raji, O., Mahmoud, M. A., Fischer, O., Ramadan, A. J., Bogachuk, D., Reinholdt, A., Schmitt, A., Kore, B. P., Gries, T. W., Musiienko, A., Schultz-Wittmann, O., Bivour, M., Hermle, M., Schubert, M. C., Borchert, J., Glunz, S. W., & Schulze, P. S. (2024). Tailoring perovskite crystallization and interfacial passivation in efficient, fully textured perovskite silicon tandem solar cells. Joule, 8(10), 2811-2833. https://doi.org/10.1016/j.joule.2024.06.018.

Even, J., Pedesseau, L., & Katan, C. (2014). Analysis of Multivalley and Multibandgap absorption and enhancement of free carriers related to exciton screening in hybrid perovskites. The Journal of Physical Chemistry C, 118(22), 11566-11572. https://doi.org/10.1021/jp503337a.

Filipoiu, N., Preda, A. T., Anghel, D., Patru, R., Brophy, R. E., Kateb, M., Besleaga, C., Tomulescu, A. G., Pintilie, I., Manolescu, A., & Nemnes, G. A. (2022). Capacitive and inductive effects in perovskite solar cells: The different roles of Ionic current and Ionic charge accumulation. Physical Review Applied, 18(6). https://doi.org/10.1103/physrevapplied.18.064087.

Gao, W., Dong, H., Sun, N., Chao, L., Hui, W., Wei, Q., Li, H., Xia, Y., Gao, X., Xing, G., Wu, Z., Song, L., Müller-Buschbaum, P., Ran, C., & Chen, Y. (2022). Chiral cation promoted interfacial charge extraction for efficient tin-based perovskite solar cells. Journal of Energy Chemistry, 68, 789-796. https://doi.org/10.1016/j.jechem.2021.09.019.

Grätzel, M. (2003). Dye-sensitized solar cells. Journal of Photochemistry and Photobiology C: Photochemistry Reviews, 4(2), 145-153. https://doi.org/10.1016/s1389-5567(03)00026-1.

Green, M. A., Dunlop, E. D., Hohl-Ebinger, J., Yoshita, M.,

Kopidakis, N., Bothe, K., Hinken, D., Rauer, M., & Hao, X. (2022). Solar cell efficiency tables (Version 60). Progress in Photovoltaics: Research and Applications, 30(7), 687-701. https://doi.org/10.1002/pip.3595.

Guo, G., & Jiang, X. (2024). Electronic structure crystallography and functional motifs of materials. John Wiley & Sons.

Guo, Y., Wu, H., Liu, Z., Shan, S., Niu, B., Lian, X., Zuo, L., & Chen, H. (2021). Manipulating perovskite precursor solidification toward 21% pristine $MAPbI_3$ solar cells. Solar RRL, 5(5). https://doi.org/10.1002/solr.202100114.

Hansen, K .R. (2023). Electroabsorption Spectroscopy of Two-Dimensional Metal Halide Perovskite. The University of Utah.

Jagadamma, L. K., & Wang, S. (2021). Wide-bandgap halide perovskites for indoor photovoltaics. Frontiers in Chemistry, 9. https://doi.org/10.3389/fchem.2021.632021.

Jeon, N. J., Noh, J. H., Kim, Y. C., Yang, W. S., Ryu, S., & Seok, S. I. (2014). Solvent engineering for high-performance inorganic–organic hybrid perovskite solar cells. Nature Materials, 13(9), 897-903. https://doi.org/10.1038/nmat4014.

Kim, D. W., Noh, Y. W., Han, J., Kim, H. S., Jang, C. H., Hong, J. A., Park, S., Lee, M. H., Kim, Y. I., & Song, M. H. (2023). Efficient $mapbi_3$-based perovskite solar cells exceeding 21% efficiency via aging treatment. Chemical Engineering Journal, 475, 146451. https://doi.org/10.1016/j.cej.2023.146451.

Kim, D., Choi, H., Jung, W., Kim, C., Park, E. Y., Kim, S., Jeon, N. J., Song, S., & Park, T. (2023). Phase transition engineering for effective defect passivation to achieve highly efficient and stable perovskite solar cells. Energy & Environmental Science, 16(5), 2045-2055. https://doi.org/10.1039/d3ee00636k.

Kim, M., Kim, G., Lee, T. K., Choi, I. W., Choi, H. W., Jo, Y., Yoon, Y. J., Kim, J. W., Lee, J., Huh, D., Lee, H., Kwak, S. K., Kim, J. Y., & Kim, D. S. (2019). Methylammonium chloride induces intermediate phase stabilization for efficient perovskite solar cells. Joule, 3(9), 2179-2192. https://doi.org/10.1016/j.joule.2019.06.014.

Kojima, A., Teshima, K., Shirai, Y., & Miyasaka, T. (2009). Organometal halide perovskites as visible-light sensitizers for photovoltaic cells. Journal of the American Chemical Society, 131(17), 6050-6051. https://doi.org/10.1021/ja809598r.

Kumar, A., & Ranjan, P. (2021). Defects signature in VOC characterization of thin-film solar cells. Solar Energy, 220, 35-42. https://doi.org/10.1016/j.solener.2021.03.017.

Kumar, J., Srivastava, P., & Bag, M. (2022). Advanced strategies to tailor the nucleation and crystal growth in hybrid halide perovskite thin films. Frontiers in Chemistry, 10. https://doi.org/10.3389/fchem.2022.842924.

Li, B., Shi, J., Lu, J., Tan, W. L., Yin, W., Sun, J., Jiang, L., Jones, R. T., Pigram, P., McNeill, C. R., Cheng, Y., & Jasieniak, J. J. (2020). Facile deposition of Mesoporous PbI_2 through DMF:DMSO solvent engineering for sequentially deposited metal halide perovskites. ACS Applied Energy Materials, 3(4), 3358-3368. https://doi.org/10.1021/acsaem.9b02391.

Li, Z., Yu, J., Xia, Y., Yang, Z., He, Y., Wang, N., & Zhu, Y. (2025). Enhanced optical modulation properties via two-step annealing of Sol–gel deposited vanadium dioxide thin films. ACS Omega, 10(4), 3691-3700. https://doi.org/10.1021/acsomega.4c08910.

Liu, X., Li, Q., Zheng, J., Xu, J., Chen, Z., Li, Z., Liu, J., Liang, S., Wang, D., Zhang, Z., Jin, X., Wu, J., & Zhang, X. (2023). Spidermen strategy for stable 24% efficiency perovskite solar cells. Advanced Functional Materials, 33(41). https://doi.org/10.1002/adfm.202308108.

Lyu, M., & Park, N. (2020). Effect of additives AX (A = FA, MA, Cs, Rb, NH4, X = Cl, BR, I) in FAPbI3 on photovoltaic parameters of perovskite solar cells. Solar RRL, 4(10). https://doi.org/10.1002/solr.202000331.

Mehri Ghasemi, Joel van Embden, Baohua Jia, & Xiaoming Wen. (2025). Author response for "Moving beyond the Shockley–queisser limit: Current bottlenecks and a new direction in solar energy conversion". https://doi.org/10.1039/d5el00053j/v2/response1.

Min, H., Lee, D. Y., Kim, J., Kim, G., Lee, K. S., Kim, J., Paik, M. J., Kim, Y. K., Kim, K. S., Kim, M. G., Shin, T. J., & Il Seok, S. (2021). Perovskite solar cells with atomically coherent interlayers on SnO2 electrodes. Nature, 598(7881), 444-450. https://doi.org/10.1038/s41586-021-03964-8.

National Renewable Energy Laboratory. (2023). Best Research-Cell Efficiency Chart. Retrieved from https://www.nrel.gov/pv/cell-efficiency.html.

Nie, W., Tsai, H., Asadpour, R., Blancon, J., Neukirch, A. J., Gupta, G., Crochet, J. J., Chhowalla, M., Tretiak, S., Alam, M. A., Wang, H., & Mohite, A. D. (2015). High-efficiency solution-processed perovskite solar cells with millimeter-scale grains. Science, 347(6221), 522-525. https://doi.org/10.1126/science.aaa0472.

Niu, T., Xue, Q., & Yip, H. (2020). Advances in Dion-Jacobson phase two-dimensional metal halide perovskite solar cells. Nanophotonics, 10(8), 2069-2102. https://doi.org/10.1515/nanoph-2021-0052.

Noh, J. H., Im, S. H., Heo, J. H., Mandal, T. N., & Seok, S. I. (2013). Chemical management for colorful, efficient, and stable inorganic–organic hybrid Nanostructured solar cells. Nano Letters, 13(4), 1764-1769. https://doi.org/10.1021/nl400349b.

Noman, M., Shahzaib, M., Jan, S. T., Khan, Z., Ismail, M., & Khan, A. D. (2024). Optimizing band gap, electron affinity, & carrier mobility for improved performance of formamidinium lead tri-iodide perovskite solar cells. Materials Science and Engineering: B, 300, 117114. https://doi.org/10.1016/j.mseb.2023.117114.

Omondi, C. A. (2018). Investigation of hybrid organic-inorganic lead halide perovskites by modulated surface photovoltage spectroscopy (AAI10830723)

[Doctoral dissertation]. ProQuest Dissertations and Theses Global.

Pandey, A., Dalal, S., Dutta, S., & Dixit, A. (2021). Structural characterization of polycrystalline thin films by X-ray diffraction techniques. Journal of Materials Science: Materials in Electronics, 32(2), 1341-1368. https://doi.org/10.1007/s10854-020-04998-w.

Panjan, P., Drnovšek, A., Čekada, M., & Panjan, M. (2022). Contamination of substrate-coating interface caused by ion etching. Coatings, 12(6), 846. https://doi.org/10.3390/coatings12060846.

Rahman, M. Z., & Edvinsson, T. (2020). X-ray diffraction and Raman spectroscopy for lead halide perovskites. Characterization Techniques for Perovskite Solar Cell Materials, 23-47. https://doi.org/10.1016/b978-0-12-814727-6.00002-5.

Sahare, S., Solovan, M. M., Mostovyi, A. I., Parkhomenko, H. P., Schopp, N., Ziółek, M., & Brus, V. V. (2025). Semiconductor Bandgap measurements: Overview of optical, electrical, and device-level techniques. Advanced Optical Materials, 13(29). https://doi.org/10.1002/adom.202501747.

Sakhatskyi, K., John, R. A., Guerrero, A., Tsarev, S., Sabisch, S., Das, T., Matt, G. J., Yakunin, S., Cherniukh, I., Kotyrba, M., Berezovska, Y., Bodnarchuk, M. I., Chakraborty, S., Bisquert, J., & Kovalenko, M. V. (2022). Assessing the drawbacks and benefits of ion migration in lead halide perovskites. ACS Energy Letters, 7(10), 3401-3414. https://doi.org/10.1021/acsenergylett.2c01663.

Sakomura, M., Yokokura, Y., Takagi, Y., & Ueda, K. (2020). Effect of insertion of bathocuproine buffer layer at grating-structured cathode–organic-layer interface in bulk-heterojunction solar cells. AIP Advances, 10(1). https://doi.org/10.1063/1.5129351.

Saliba, M., Matsui, T., Seo, J., Domanski, K., Correa-Baena, J., Nazeeruddin, M. K., Zakeeruddin, S. M., Tress, W., Abate, A., Hagfeldt, A., & Grätzel, M. (2016). Cesium-containing triple cation perovskite solar cells: Improved stability, reproducibility and high efficiency. Energy & Environmental Science, 9(6), 1989-1997. https://doi.org/10.1039/c5ee03874j.

Shaik, F., Lingala, S. S., & Veeraboina, P. (2023). Effect of various parameters on the performance of solar PV power plant: A review and the experimental study. Sustainable Energy Research, 10(1). https://doi.org/10.1186/s40807-023-00076-x.

Shao, S., & Loi, M. A. (2021). Advances and prospective in metal halide Ruddlesen–Popper perovskite solar cells. Advanced Energy Materials, 11(11). https://doi.org/10.1002/aenm.202003907.

Sivakumar, N., Saha, S., Madaka, R., Bandaru, N., & Rath, J. K. (2023). Investigation on the structural, spectral, and optical properties of $MAPbI_3$.H2O and $MAPbI_3$ perovskite crystals for photovoltaic cells. Journal of Materials Science: Materials in Electronics, 34(15). https://doi.org/10.1007/s10854-023-10607-3.

Soltani, S., Hjiri, M., Ahmed, N. I., Jbeli, A., Aldukhayel, A. M., & Althumairi, N. A. (2025). Metal halide perovskites for energy applications: Recent advances, challenges, and future perspectives. RSC Advances, 15(27), 21811-21837. https://doi.org/10.1039/d5ra02730f.

Stranks, S. (2020). An emerging solar photovoltaic technology poised to revolutionise energy generation. https://doi.org/10.33774/coe-2020-47fh3.

Subha, T. D., Prabu, R. T., Parasuraman, S., & Kumar, A. (2023). Role of Urbach energy in controlling voltage output of solar cells. Optical and Quantum Electronics, 55(9), 794. https://doi.org/10.1007/s11082-023-05067-2.

Tan, D., Jiang, C., Li, Q., Bi, S., & Song, J. (2020). Silver nanowire networks with preparations and applications: a review. Journal of Materials Science: Materials in Electronics, 31(18), 15669-15696. https://doi.org/10.1007/s10854-020-04131-x.

Tan, W. L., & McNeill, C. R. (2022). X-ray diffraction of photovoltaic perovskites: Principles and applications. Applied Physics Reviews, 9(2). https://doi.org/10.1063/5.0076665.

Tipparak, P., Passatorntaschakorn, W., & Thongratanakul, S. (2025). The impact of $MAPbI_3$ quantum dots on CsFA perovskite solar cells: Interface and hole extraction improvement, ACS Applied Energy Materials, 8(1), 355–364. https://doi.org/10.1021/acsaem.4c02474.

Tonui, P., Oseni, S. O., Sharma, G., Yan, Q., & Mola, G. T. (2018). Perovskites photovoltaic solar cells: An overview of current status. Renewable and Sustainable Energy Reviews, 91, 1025-1044. https://doi.org/10.1016/j.rser.2018.04.069.

Traiwattanapong, W., Molahalli, V., Pattanaporkratana, A., & Chattham, N. (2024). Recent Developments in Thermally Stable Transparent Thin Films for Heater Applications: A Systematic Review. Nanomaterials, 14(24), 2011. https://doi.org/10.3390/nano14242011.

Ulhakim, M. T., Sukarman, S., Khoirudin, K., Fazrin, N., Irfani, T., & Hakim, A. (2024). Determining the crystallite size of TiO2/EG-water XRD data using the Scherrer equation. INDONESIAN JOURNAL OF APPLIED PHYSICS, 14(1), 141. https://doi.org/10.13057/ijap.v14i1.79195.

Unger, E. L., Hoke, E. T., Bailie, C. D., Nguyen, W. H., Bowring, A. R., Heumüller, T., … McGehee, M. D. (2014). Hysteresis and transient behavior in current-voltage measurements of hybrid-perovskite absorber solar cells. Energy & Environmental Science, 7(11), 3690–3698. Retrieved May 10, 2025 from https://pubs.rsc.org/en/content/articlelanding/2014/ee/c4ee02465f.

Wanyonyi, S., Omogo, B., Awino, C., Shatsala, M., Nalianya, M. A., Lisouza, F. A., Odhiambo, A. S., & Gaitho, F. M. (2024). Crystallization dynamics of $MAPbI_3$ perovskite solar cells via solvent engineering methods. South Florida Journal of Development, 5(11), e4623. https://doi.org/10.46932/sfjdv5n11-024.

Wei, Q., Wang, N., Gao, Y., Zhuansun, Y., Wang, J., Zhu,

D., Zan, L., Fu, F., & Liu, Y. (2024). Elevated efficiency and stability of hole-transport-Layer-Free perovskite solar cells triggered by surface engineering. ACS Applied Materials & Interfaces. https://doi.org/10.1021/acsami.4c01892.

Williamson, G. K., & Hall, W. H. (1953). X-ray line broadening from field aluminium and wolfram. Acta Metallurgica, 1(1), 22–31. https://doi.org/10.1016/0001-6160(53)90006-6.

Wu, T., Wang, P., Zheng, L., Zhao, Y., & Hua, Y. (2024). Perovskite crystallization and hot carrier dynamics manipulation enables efficient and stable perovskite solar cells with 25.32% efficiency (Adv. Energy mater. 24/2024). Advanced Energy Materials, 14(24). https://doi.org/10.1002/aenm.202470099.

Xing, G., Mathews, N., Sun, S., Lim, S. S., Lam, Y. M., Grätzel, M., Mhaisalkar, S., & Sum, T. C. (2013). Long-range balanced electron- and hole-transport lengths in organic-inorganic CH3NH3PbI3. Science (New York, N.Y.), 342(6156), 344–347. https://doi.org/10.1126/science.1243167.

Yu, Z., Wang, J., Chen, B., Uddin, M. A., Ni, Z., Yang, G., & Huang, J. (2022). Solution-processed ternary tin (II) alloy as hole-transport layer of Sn–PB perovskite solar cells for enhanced efficiency and stability. Advanced Materials, 34(49). https://doi.org/10.1002/adma.202205769.

Zanatta, A. R. (2022). The Shockley–Queisser limit and the conversion efficiency of silicon-based solar cells. Results in optics, 9, 100320. https://doi.org/10.1016/j.rio.2022.100320.

Zhang, F., Park, S. Y., Yao, C., Lu, H., Dunfield, S. P., Xiao, C., … Zhu, K. (2022). Metastable Dion-Jacobson 2D structure enables efficient and stable perovskite solar cells. Science, 375(6576), 71–76. https://doi.org/10.1126/science.abj2637.

Zhang, J., Wang, H., Yang, Q., Gao, C., Gao, C., & Liu, X. (2023). Ultrathin SnO2 electron transport layers for perovskite solar cells by combustion method at low temperature. Optical Materials, 137, 113518. https://doi.org/10.1016/j.optmat.2023.113518.